Title

Cancer-cell-secreted extracellular vesicles target p53 to impair mitochondrial function in muscle

Journal

EMBO Reports, 24(9)

ISSN

1469-221X

Authors

Ruan, Xianhui

Cao, Minghui

Yan, Wei

et al.

Publication Date

2023-09-06

DOI

10.15252/embr.202256464

Peer reviewed

Article

TRANSPARENT PROCESS

EMBO reports

Cancer-cell-secreted extracellular vesicles target p53 to impair mitochondrial function in muscle

Xianhui Ruan[1], Minghui Cao[1], Wei Yan[1], Ying Z Jones[2], Åsa B Gustafsson[3], Hemal H Patel[4,5], Simon Schenk[6] & Shizhen Emily Wang[1,7,*]

Abstract

Skeletal muscle loss and weakness are associated with bad prognosis and poorer quality of life in cancer patients. Tumor-derived factors have been implicated in muscle dysregulation by inducing cachexia and apoptosis. Here, we show that extracellular vesicles secreted by breast cancer cells impair mitochondrial homeostasis and function in skeletal muscle, leading to decreased mitochondrial content and energy production and increased oxidative stress. Mechanistically, miR-122-5p in cancer-cell-secreted EVs is transferred to myocytes, where it targets the tumor suppressor TP53 to decrease the expression of TP53 target genes involved in mitochondrial regulation, including Tfam, Pgc-1α, Sco2, and 16S rRNA. Restoration of Tp53 in muscle abolishes mitochondrial myopathology in mice carrying breast tumors and partially rescues their impaired running capacity without significantly affecting muscle mass. We conclude that extracellular vesicles from breast cancer cells mediate skeletal muscle mitochondrial dysfunction in cancer and may contribute to muscle weakness in some cancer patients.

Keywords breast cancer; extracellular vesicles; microRNA; p53; skeletal muscle

Subject Categories Cancer; Membrane & Trafficking; Metabolism

DOI 10.15252/embr.202256464 | Received 10 November 2022 | Revised 27 June 2023 | Accepted 30 June 2023 | Published online 13 July 2023

EMBO Reports (2023) 24: e56464

Introduction

Despite the advances in early detection and treatment over the last decade, breast cancer (BC) remains the most commonly diagnosed cancer in women worldwide and the second leading cause of cancer mortality in American women (Noone *et al*, 2018; Siegel *et al*, 2018). Compared to healthy women, over one-thirds of non-metastatic BC patients have lower skeletal muscle mass at diagnosis (Caan *et al*, 2018), and about two-thirds of metastatic BC patients present with reduced muscle mass and poor muscle quality (Rier *et al*, 2017). Loss of skeletal muscle and poor muscle quality are associated with increased risk of death in BC patients (Prado *et al*, 2009; Villasenor *et al*, 2012; Rier *et al*, 2017; Shachar *et al*, 2017; Caan *et al*, 2018). This could be partially attributed to poor tolerance and response to chemotherapy in patients with pre-therapeutic low muscle mass (Prado *et al*, 2009; Shachar *et al*, 2017; Pamoukdjian *et al*, 2018). Therefore, understanding how BC influences skeletal muscle homeostasis and functionality is of utmost importance to improve patient's cancer prognosis and quality of life. Recent studies have started to elucidate BC-induced reprogramming of skeletal muscle using human muscle biopsies (Wilson *et al*, 2020) and mouse muscle from patient-derived xenograft model (Wilson *et al*, 2019), revealing aberrant mitochondrial function and altered signaling pathways such as peroxisome proliferator-activated receptor (PPAR), mechanistic target of rapamycin (mTOR), and interleukin 6 (IL-6), which potentially contribute to muscle fatigue.

Previous studies on mechanisms of cancer-induced cachexia, which involves skeletal muscle loss and systemic inflammation, have revealed that tumor-derived or tumor-induced, host-derived proinflammatory cytokines (including tumor necrosis factor (TNF)-α and IL-6) are associated with cachexia (Fearon *et al*, 2012). Bone-released factors such as transforming growth factor (TGF)-β induce muscle weakness but only in the setting of bone metastasis (Waning *et al*, 2015). Cancer-secreted extracellular vesicles (EVs), which can travel to various organs through the circulation are an emerging group of effectors that mediate cancer's systemic effects including cachexia. Recent studies have revealed cachexia-inducing effects of EV cargo miR-21 and chaperon proteins (Hsp70 and Hsp90) through activation of Toll-like receptors to, respectively, promote myoblast apoptosis and muscle catabolism (He *et al*, 2014; Zhang *et al*, 2017). However, these mechanisms are observed only with EVs from certain cancer types such as lung and pancreas, but not with BC-derived EVs that do not exhibit high levels of miR-21 or Hsp70/90 (He *et al*, 2014; Zhang *et al*, 2017). Here, we report a mechanism of mitochondrial dysregulation by BC-

1 Department of Pathology, University of California San Diego, La Jolla, CA, USA
2 Department of Cellular & Molecular Medicine, University of California San Diego, La Jolla, CA, USA
3 Skaggs School of Pharmacy and Pharmaceutical Sciences, University of California San Diego, La Jolla, CA, USA
4 VA San Diego Healthcare System, San Diego, CA, USA
5 Department of Anesthesiology, University of California San Diego, La Jolla, CA, USA
6 Department of Orthopedic Surgery, University of California San Diego, La Jolla, CA, USA
7 Moores Cancer Center, University of California San Diego, La Jolla, CA, USA
*Corresponding author. Tel: +01 858 246 2464; E-mail: emilywang@ucsd.edu

secreted, EV-encapsulated miR-122, which causes suppression of p53 signaling in skeletal muscle.

Skeletal muscle depends heavily on ATP generated by aerobic respiration, and mitochondrial dysfunction has been associated with a variety of muscle disorders (Lowell & Shulman, 2005; Montgomery & Turner, 2015). Decreased electron flow through the electron transport chain (ETC) can cause electron leakage and formation of reactive oxygen species (ROS), leading to cell damage followed by mitophagy or apoptosis (Montgomery & Turner, 2015). The production of ATP in mitochondria is coordinated with the contractile activity of muscle through the propagation of Ca^{2+} spikes from cytoplasm to mitochondrial matrix to stimulate energy production (Griffiths & Rutter, 2009). The tumor suppressor p53 has been linked to muscle metabolism and function with a particularly important role in maintaining normal mitochondrial function. p53 impacts cell energy homeostasis by promoting oxidative phosphorylation (OXPHOS) and mitochondrial biogenesis. It regulates the expression of several genes critical to mitochondrial homeostasis and function. Among these genes, PGC-1α (peroxisome proliferator-activated receptor γ coactivator 1-α) is a master regulator of mitochondrial biogenesis (Ruas *et al*, 2012; Aquilano *et al*, 2013). p53 also regulates several nuclear-encoded mitochondrial proteins, including TFAM (transcription factor A, mitochondrial; mtTFA) that is essential to the maintenance and transcription of mitochondrial DNA (mtDNA) (Park *et al*, 2009; Wen *et al*, 2016), SCO2 (synthesis of cytochrome c oxidase 2) that controls the assembly of cytochrome c oxidase (COX) complex/Complex IV in the respiratory ETC (Matoba *et al*, 2006), and the mitochondrial 16S ribosomal RNA (16S rRNA) that is critical to the translation of mtDNA-encoded genes (Donahue *et al*, 2001). The skeletal muscle of *Trp53* whole-body knockout (KO) mice exhibits reduced PGC-1α level and reduced mitochondrial and mtDNA contents as well as impaired mitochondrial morphology and function, including altered ultrastructure, reduced respiration and complex IV assembly, and elevated ROS production in intermyofibrillar (IMF) mitochondria that generate ATP needed for contraction (Park *et al*, 2009; Saleem *et al*, 2009, 2015). These KO mice exhibit greater fatigability and lower exercise capacity compared to wild-type controls (Park *et al*, 2009; Saleem *et al*, 2009). However, these effects are absent in a mouse model with skeletal muscle-specific loss of *Trp53* under basal conditions (Stocks *et al*, 2017), highlighting the need to dissect the direct and indirect effects of p53 in mature skeletal muscle and under a pathological context, such as cancer. Here, we establish a miRNA-mediated mechanism through which cancer-cell-derived EVs regulate p53 expression and signaling in skeletal muscle, which subsequently leads to impairment of mitochondrial function and energy production in skeletal muscle.

Results

EVs of BC cells suppress p53 signaling and gene expression related to mitochondrial homeostasis and function

We first used an intravenous (i.v.) EV injection model of female NOD/SCID/IL2Rγ-null (NSG) mice to assess the systemic effects of administered EVs in circulation. Several EV markers, but not a Golgi marker, were detected in the EVs used in this study (Fig EV1A). Nanoparticle tracking analysis (NTA) confirmed the typical size distribution of an exosome-containing EV preparation (Fig EV1B). To assess the topological localization of EV cargo such as selected miRNA, we treated EVs with protease followed by RNase to remove extra-EV RNA prior to measurement of the miRNA and compared the miRNA levels to those in untreated EVs (Fig EV1C). To determine if EVs administered via tail vein injections can travel to skeletal muscle, we tracked EVs derived from MCF-10A non-cancer mammary epithelial cells or MDA-MB-231 BC cells stably expressing a membrane-targeted Lck-GFP (Benediktsson *et al*, 2005). EVs produced by these cells contained Lck-GFP to allow *in vivo* tracking. After 5 weeks of semiweekly EV injections, fluorescent microscopy of *gastrocnemius* (GA) cross-sections showed GFP signals in a significant subset of muscle cells for both EV-producing cell lines (Fig 1A). Therefore, circulating EVs can indeed enter skeletal muscle cells to exert a

Figure 1. BC-cell-derived EVs suppress the p53 pathway in skeletal muscle through miR-122.

A GFP signals in GA from NSG mice receiving tail vein injections of Lck-GFP-labeled EVs derived from MCF-10A or MDA-MB-231 cells. Scale bar: 100 μm.
B The entire GA collected from mice that had received indicated EVs for 5 weeks were analyzed by RNA-seq. GSEA shows enrichment of genes related to indicated pathways (n = 5 mice for MDA-MB-231 EVs and n = 4 mice for MCF-10A/vec EVs). NES, normalized enrichment score.
C Western blot showing p53 protein levels in C2C12 myotubes treated with EVs or PBS and transfected with indicated anti-miRNAs.
D GSEA of RNA-seq data comparing GA from mice that had received EVs from MCF-10A/vec or MCF-10A/miR-122 cells for 5 weeks (n = 5 mice for MCF-10A/miR-122 EVs and n = 4 mice for MCF-10A/vec EVs).
E Western blot analysis showing protein levels of p53 and genes related to mitochondrial homeostasis and function in GA of mice receiving PBS or indicated EVs.
F RT–qPCR showing relative levels of miR-122 and indicated mRNAs in GA of indicated groups of mice. Data were normalized to U6 (for miR-122) or *Ppib* (for all mRNAs) and compared to control group receiving PBS (one-way ANOVA, n = 4 or 5 mice per group).
G Relative mtDNA/nDNA ratio in GA determined by PCR (one-way ANOVA, n = 4 mice per group).
H ROS levels in GA from indicated groups of mice detected by DHE staining (red). DAPI (blue) shows the nuclei. Quantified DHE signals were normalized to DAPI signals on the same section and used in analysis (one-way ANOVA, n = 4 mice per group). Scale bar: 50 μm.
I ROS levels in GA from mice that had received indicated EV treatment for 5 weeks. Quantified DHE signals were normalized to DAPI signals on the same section and used in analysis (one-way ANOVA, n = 4 mice per group). Scale bar: 50 μm.
J RT–qPCR showing relative levels of indicated mRNAs in GA of indicated groups of mice (one-way ANOVA, n = 5 mice per group).
K Relative mtDNA/nDNA ratio in GA determined by PCR (one-way ANOVA, n = 5 mice per group).
L Treadmill running test of mice that had received indicated EV treatment for 5 weeks (one-way ANOVA, n = 4 mice per group).

Data information: In bar graphs, values are shown as mean ± SD. The boxes in the box-and-whiskers plots show the median (center line) and the quartile range (25–75%), and the whiskers extend from the quartile to the minimum and maximum values. *P < 0.05, **P < 0.01, ***P < 0.001, ns: not significant. Western blot signals are quantified and normalized to Gapdh.

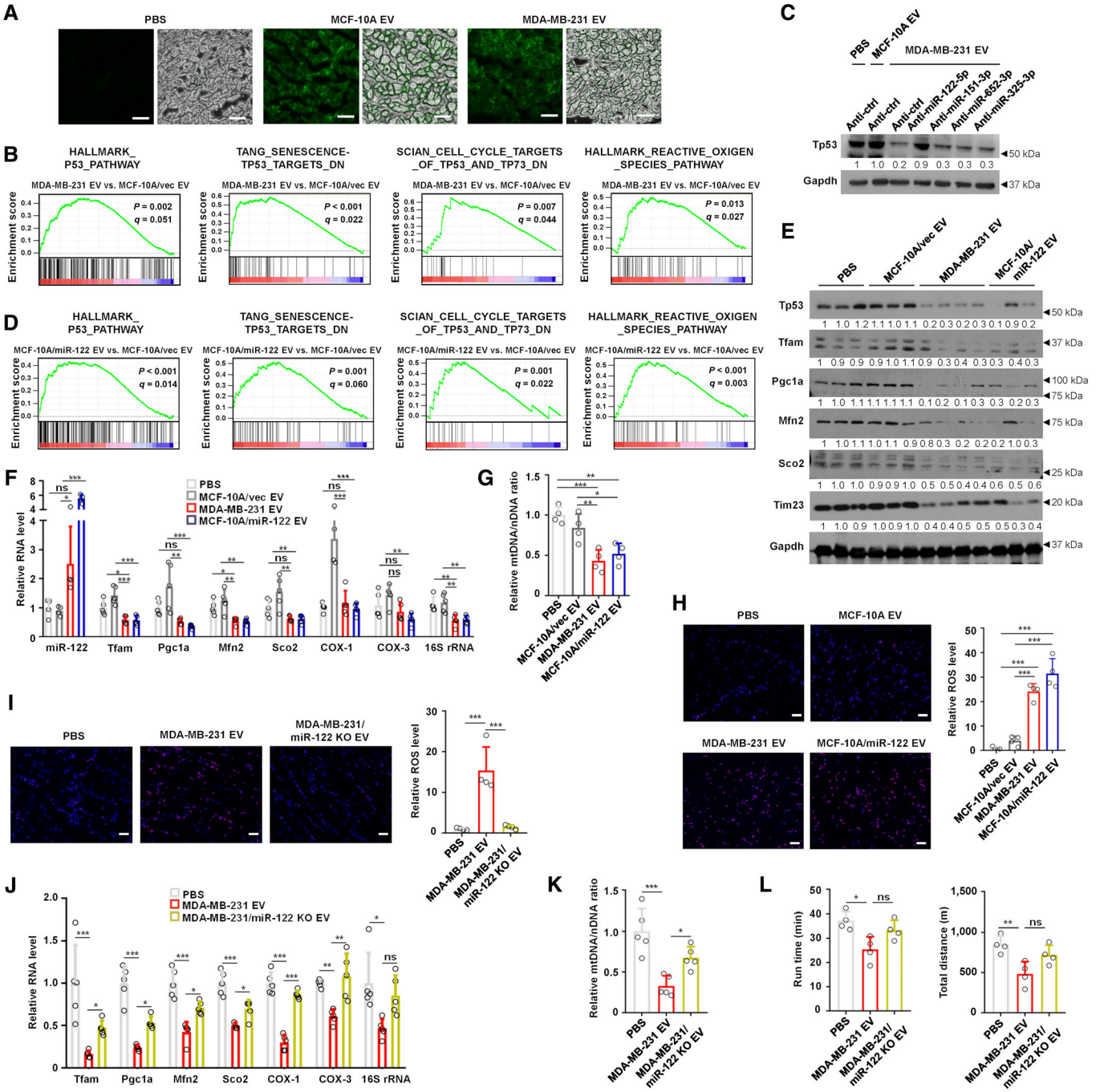

Figure 1.

direct effect; nevertheless, other indirect mechanisms through paracrine or endocrine signaling are also possible.

We then i.v. administered female NSG mice with an equal amount of unlabeled (no GFP) EVs from MCF-10A or MDA-MB-231 cells for a total of 5 weeks at a semiweekly frequency. Compared to mice receiving MCF-10A EVs, those receiving MDA-MB-231 EVs showed decreased weights of GA and tibialis muscle (Fig EV2A) and wide spacing of muscle fibers (Fig EV2B). We used the entire GA for transcriptomic profiling by RNA-seq followed by gene set enrichment analysis (GSEA; Dataset EV1), which revealed significant downregulation of p53 pathway and ROS induction in mice receiving MDA-MB-231 EVs compared to those receiving the experimental control, MCF-10A EVs (Fig 1B). Previous studies have linked p53 signaling to maintenance of mitochondrial homeostasis and function in non-cancer tissues including skeletal muscle (Park *et al*, 2009; Saleem *et al*, 2009, 2015). Recent transcriptomic and proteomic analyses of skeletal muscle biopsies from BC patients and non-cancer controls also indicate BC-induced mitochondrial dysfunction regardless of treatment history or tumor molecular subtype (Wilson *et al*, 2020). Therefore, in the current study, we focused on BC-induced

mitochondrial dysregulation in skeletal muscle as a potential consequence of EV-mediated p53 downregulation.

To determine the mechanism of p53 downregulation, we explored miRNAs that potentially target p53 by inquiring about the TargetScan algorithm. Human TP53 ENST00000420246.2, which contains the longest (1496-nt) 3′UTR among all TP53 transcripts, shows multiple species-conserved miRNA-binding sites (Dataset EV2). Among these, eight are present at a higher level in the EVs from MDA-MB-231 compared to those from MCF-10A cells based on our previously published dataset (Zhou *et al*, 2014), with miR-122-5p (miR-122) showing the highest secretion by cancer cells. Additionally, three of these eight miRNAs have conserved sites in mouse *Trp53* (Dataset EV2), and therefore might mediate the downregulation of p53 in mouse skeletal muscle. We tested these three miRNAs (miR-122-5p, miR-151-3p, and miR-652-3p) as well as miR-325-3p (as a control not significantly secreted by MDA-MB-231 cells) by using anti-miRNAs to individually block their effect in EV-treated C2C12 myotubes. Only the blockade of miR-122 abolished p53 downregulation by MDA-MB-231 EVs (Fig 1C), indicating miR-122 was the main effector mediating this regulation by cancer-derived EVs. We previously reported that miR-122 is highly secreted by BC cells compared to non-cancer cells and promotes BC metastasis by downregulating glycolysis in non-cancer cells (Fong *et al*, 2015), and that a higher level of circulating miR-122 is associated with therapeutic resistance and metastatic relapse in BC patients (Wu *et al*, 2012). Levels of EV-associated miR-122 were unaffected by treating MDA-MB-231 EVs with protease followed by RNase, but were reduced by > 50% when the treatment was conducted in 1% Triton X-100 to destroy membrane structure, indicating a majority of miR-122 was inside BC-derived EVs (Fig EV1C). Relevant to this study, *TP53* mRNA contains a putative miR-122-binding site, which was confirmed to mediate downregulation of p53 in our subsequent experiments. Similar to MDA-MB-231 EVs, i.v. injected high-miR-122 EVs derived from miR-122-overexpressing MCF-10A cells also suppressed p53 pathway and induced ROS pathway in skeletal muscle (Fig 1D). Western blot and RT–qPCR assays of skeletal muscle further confirmed that EVs from both MDA-MB-231 and MCF-10A/miR-122 cells, compared to MCF-10A EVs or PBS control treatment, led to reductions in p53 protein and the expression of its target genes that are known to mediate mitochondrial homeostasis and function, including Tfam, Pgc-1α, Mfn2, and Sco2 (Fig 1E and F). This was accompanied by decreased mtDNA contents (Fig 1G) and increased ROS levels (Fig 1H). In contrast, in this model, we did not observe significant regulation of the two E3 ligases, muscle atrophy F-box protein (atrogin-1) and muscle RING finger 1 (MuRF1), as well as autophagy marker LC3b in the muscle as an effect of cancer EVs (Fig EV3A and B). We did not observe any significant effect of MDA-MB-231 EVs on body weight (Cao *et al*, 2022), food consumption (Cao *et al*, 2022), O_2 consumption, CO_2 production, or respiratory exchange ratio (Fig EV4). We further examined the effect of miR-122-depleted EVs from MDA-MB-231 cells with CRISPR-Cas9-mediated genetic ablation of *hsa-mir-122* (MDA-MB-231/miR-122 KO cells). Unlike MDA-MB-231 EVs, i.v. administration of MDA-MB-231/miR-122 KO EVs did not significantly alter ROS levels, p53 target gene expression, or mtDNA contents in the muscle (Fig 1I–K). In a treadmill running test, mice receiving MDA-MB-231 EVs but not the miR-122 KO EVs exhibited decreased total running time and distance compared to the PBS-treated control group (Fig 1L). Our data thus far collectively suggest BC-derived EVs may exert an effect on skeletal muscle through mitochondrial dysregulation, which may result from miR-122-mediated downregulation of p53.

miR-122 in BC-derived EVs targets p53 to suppress mitochondrial function in myotubes

The TargetScan-predicted miR-122-binding site, which is located at position 200–206 of the 3′UTR of human TP53 ENST00000420246.2 transcript, corresponds to position 1235–1241 in the CDS region of NM_000546 human TP53 transcript variant 1 mRNA, about 90 bps upstream of the stop codon (Fig 2A and B). A luciferase reporter construct that contains a 340 bp region of human *TP53* cDNA encompassing the miR-122 site responded to transfected miR-122 mimic with downregulated luciferase expression; this was abolished when the miR-122 site was mutated in the reporter (Fig 2B and C). We further studied the effect of EV-transferred miR-122 in C2C12 myotubes, which exhibited efficient uptake of EVs from MCF-10A and MDA-MB-231 cells (Fig 2D). EVs with high levels of miR-122, including those from MDA-MB-231 and MCF-10A/miR-122 cells, suppressed the expression levels of p53, Tfam, Pgc-1α, Mfn2, and Sco2 in C2C12 (Fig 3A and B). Following treatment with high-miR-122 EVs, C2C12 myotubes also showed reduced intracellular ATP levels (Fig 3C) and elevated ROS levels (Fig 3D), consistent with a suppressed mitochondrial function. In contrast, EVs from MDA-MB-231/miR-122 KO cells did not have these effects, whereas transfection of a miR-122 mimic recapitulated the effects of high-miR-122 EVs (Fig 3A–D). Overexpression of a human *TP53* cDNA construct that carries a silent mutation to disrupt the miR-122-binding site without affecting the amino acid coding indeed increased the expression of these p53 target genes related to mitochondrial function (Fig 3A). In addition, exogenous expression of this miR-122-resistent *TP53* construct abolished the effects of miR-122 on p53 target gene expression and intracellular levels of ATP and ROS (Fig 3A, C and D). These results in myotubes, together with the data from skeletal muscle (Fig 1), suggest the effects of BC-derived EVs on p53 signaling and muscle mitochondrial function are mediated by miR-122-dependent downregulation of p53. miR-122 has also been reported to target IGF1R and thereby regulate the PI3K/Akt/mTOR/p70S6K pathway in BC cells (Wang *et al*, 2012). However, likely due to the highly context-dependent miRNA targeting and function, our GSEA analysis of mouse skeletal muscle indicated that cancer cell-derived EVs (MDA-MB-231 EVs) or EVs from MCF-10A/miR-122 cells do not affect the IGF1/mTOR pathway (Fig EV5A). We also did not observe suppression of the PI3K/Akt pathway in western blot analysis of skeletal muscle from tumor-bearing mice (Fig EV5B).

Tumors defective in EV secretion or miR-122 expression fail to dysregulate p53 and mitochondria in the muscle

To determine if the effects described above can be caused by primary tumor-derived EVs during the course of tumor growth, we used a xenograft tumor model of MDA-MB-231 by injecting cancer cells into the mammary fat pad of female NSG mice. To further evaluate the requirements of EV secretion and miR-122 as parts of the proposed mechanism, we also established xenograft tumors using MDA-MB-231 cells with stable knockdown of Rab27a, a small GTPase essential

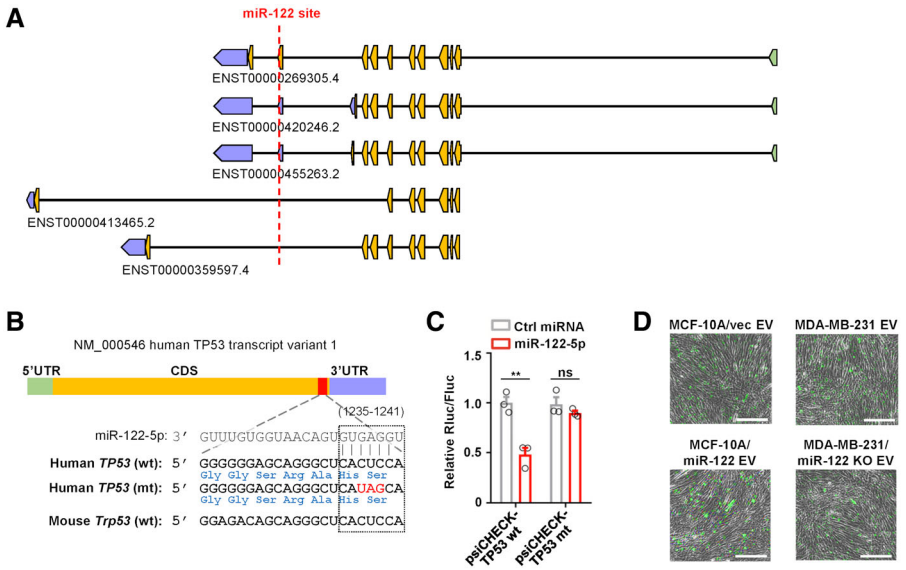

Figure 2. The predicted miR-122-binding site in p53 transcripts is confirmed in myotubes.

A The respective position of TargetScan-predicted miR-122-binding site in various human TP53 transcripts.

B Predicted miR-122-binding site in NM_000546 human TP53 transcript variant 1 mRNA and the corresponding region in mouse gene transcript. Sequences in wild-type (wt) and mutated (mt) reporters are shown.

C Responsiveness of the reporters to miR-122 mimic in transfected C2C12 (*t*-test, $n = 3$ biological replicates).

D CFSE signals in C2C12 myotubes treated with indicated CFSE-labeled EVs for 24 h, indicating EV uptake. Scale bar: 100 μm.

Data information: In bar graph, values are shown as mean ± SD. $^{**}P < 0.01$, ns: not significant.

for exosome secretion (Ostrowski *et al*, 2010), as well as MDA-MB-231 cells with miR-122 knockout. Skeletal muscle from mice-bearing MDA-MB-231-derived mammary tumors showed human CD63 immunofluorescence signals in a significant subset of Myogenin$^+$ myocytes (Fig 4A), confirming the *in vivo* uptake of tumor-derived EVs. Similar to mice that have received high-miR-122 EVs, mice-bearing MDA-MB-231 tumors, compared with tumor-free controls, had reduced expression of p53 pathway components and higher levels of miR-122 (Fig 4B–D) as well as reduced levels of mtDNA (Fig 4E) and lower contents of subsarcolemmal (SS) and intermyofibrillar (IMF) mitochondria (Fig 4F) in the skeletal muscle. In addition, these mice also had decreased total running time and distance on a treadmill running test (Fig 4G). Of note, all these effects were abolished when the tumor was defective in EV secretion (the Rab27a KD tumors) or lacked miR-122 (the miR-122 KO tumors; Fig 4B–G). Using a 4 T1 orthotopic tumor model, we observed similar EV- and miR-122-dependent effects on p53 pathway and mtDNA in the skeletal muscle in female BALB/c mice (Fig 4H–J). These results suggest that the dysregulation of p53 signaling and mitochondrial function in the skeletal muscle of tumor-bearing mice depends on EV secretion by BC cells and BC-derived miR-122. The downregulation of multiple p53 target genes and mtDNA content by cancer cell-derived EVs was further confirmed in female NSG mice receiving EVs from SKBR3 BC cells via i.v. injections (Fig 5A–C). We thereby propose a mechanistic model in which cancer cell-derived EVs that carry a high level of miR-122 travel to the skeletal muscle through the circulation and downregulate p53 pathway in myocytes, which results in decreased gene expression related to mitochondrial homeostasis, reduced mitochondrial contents, and impaired mitochondrial function and energy production.

Restoration of p53 expression in skeletal muscle rescues mitochondrial content in tumor-bearing mice

To further support our proposed model, we performed *in vivo* restoration of p53 expression using adeno-associated virus 8 (AAV8) constructed to express the miR-122-resistant TP53. Female NSG mice first received injections of MDA-MB-231 cells into the

Figure 3. miR-122 directly targets p53 to dysregulate mitochondria in myotubes.

A Western blot showing levels of indicated proteins in C2C12 treated with indicated EVs, or transfected as indicated with miR-122 mimic or TP53 expression plasmid carrying silent mutation of the miR-122-binding site.

B RT–qPCR of indicated genes in treated C2C12. Data were normalized to *Ppib* and compared to the control group (PBS treatment) (one-way ANOVA, $n = 3$ biological replicates).

C Relative ATP levels in C2C12 myotubes treated as indicated (one-way ANOVA, $n = 3$ biological replicates).

D Relative ROS levels in C2C12 myotubes treated as indicated (one-way ANOVA, $n = 3$–5 biological replicates).

Data information: In bar graphs, values are shown as mean ± SD. $^{*}P < 0.05$, $^{**}P < 0.01$, and $^{***}P < 0.001$, ns: not significant. Western blot signals are quantified and normalized to Gapdh.

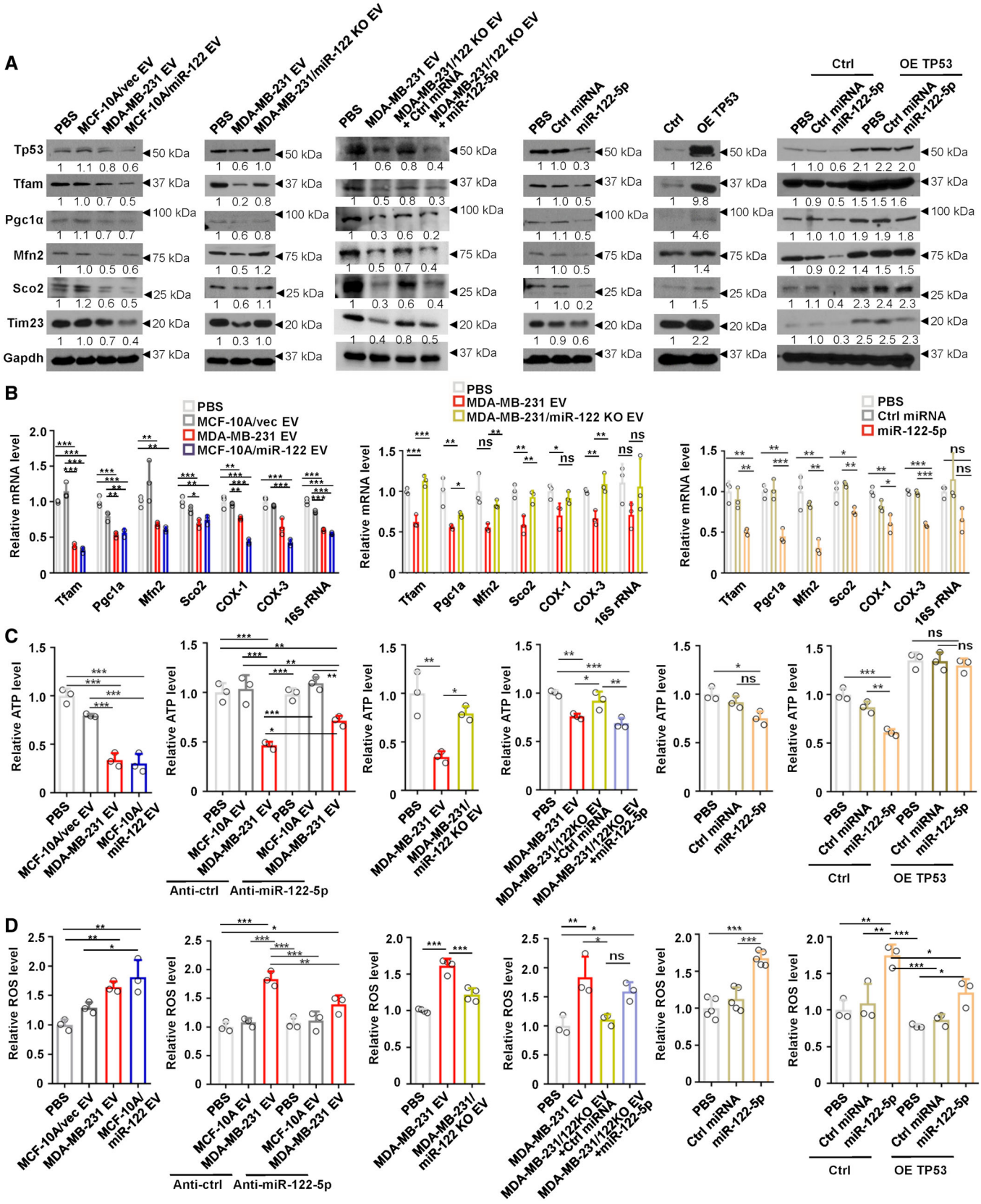

Figure 3.

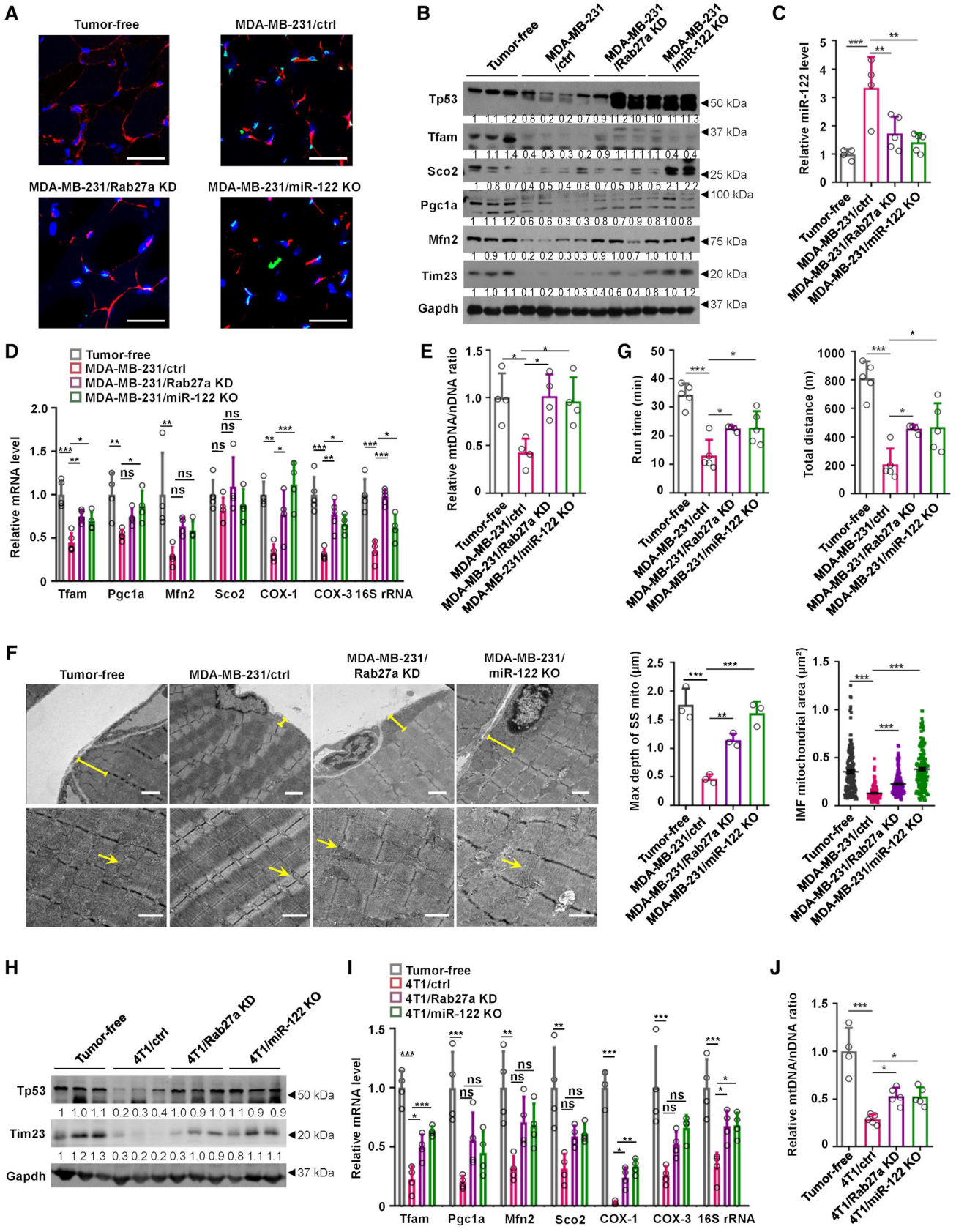
A
Tumor-free
MDA-MB-231/ctrl
MDA-MB-231/Rab27a KD
MDA-MB-231/miR-122 KO
B
Tumor-free
MDA-MB-231/ctrl
MDA-MB-231/Rab27a KD
MDA-MB-231/miR-122 KO
Tp53
Tfam
Sco2
Pgc1a
Mfn2
Tim23
Gapdh
50 kDa
37 kDa
25 kDa
100 kDa
75 kDa
20 kDa
37 kDa
C
Relative miR-122 level
D
Relative mRNA level
Tfam
Pgc1a
Mfn2
Sco2
COX-1
COX-3
16S rRNA
E
Relative mtDNA/nDNA ratio
G
Run time (min)
Total distance (m)
F
Max depth of SS mito (μm)
IMF mitochondrial area (μm²)
H
4T1/ctrl
4T1/Rab27a KD
4T1/miR-122 KO
I
Relative mRNA level
J
Relative mtDNA/nDNA ratio

Figure 4.

Figure 4. Tumors require EV secretion and miR-122 to suppress the p53 pathway and mitochondrial content in skeletal muscle.

A Immunofluorescence images showing human CD63 (green), Myogenin (red), and DAPI (blue) signals in GA from NSG mice carrying indicated xenograft tumors or no tumor (the tumor-free group). For all three tumor-bearing groups, GA was collected when tumor volume reached ~400 mm^3. Scale bar: 50 μm.

B Indicated MDA-MB-231-derived BC cells were injected into the mammary fat pad of female NSG mice to form tumors. Tumor-bearing and age-matched tumor-free mice were sacrificed for muscle collection at week 6. Western blots show protein levels in GA.

C, D RT–qPCR showing relative levels of miR-122 (C) and indicated mRNAs (D) in GA of tumor-free and tumor-bearing mice. Data were normalized to U6 (for miR-122) or *Ppib* (for all mRNAs) and compared to the tumor-free group (one-way ANOVA, $n = 4$ or 5 mice per group).

E Relative mtDNA/nDNA ratio in GA determined by PCR (one-way ANOVA, $n = 4$ mice per group).

F Representative TEM images showing SS and IMF mitochondria and their quantification in GA (one-way ANOVA, $n = 3$ mice per group for the left subpanel and $n = 154$–164 mitochondria analyzed per group for the right subpanel). Scale bar: 1 μm. Yellow bars: depths of SS mitochondrial areas; arrows: IMF mitochondrial area.

G Total running time and distance measured at week 6 in a run-to-exhaustion treadmill test (one-way ANOVA, $n = 4$ or 5 mice).

H Western blots of GA from female BALB/c mice-bearing 4 T1-derived tumors with tumor-free mice as controls.

I RT–qPCR showing levels of indicated genes of GA from indicated BALB/c mice (one-way ANOVA, $n = 4$ or 5 mice).

J Ratio of mtDNA/nDNA in GA from indicated BALB/c mice (one-way ANOVA, $n = 4$ or 5 mice).

Data information: In bar graphs, values are shown as mean ± SD. The boxes in the box-and-whiskers plots show the median (center line) and the quartile range (25–75%), and the whiskers extend from the quartile to the minimum and maximum values. *$P < 0.05$, **$P < 0.01$, ***$P < 0.001$, ns: not significant. Western blot signals are quantified and normalized to Gapdh.

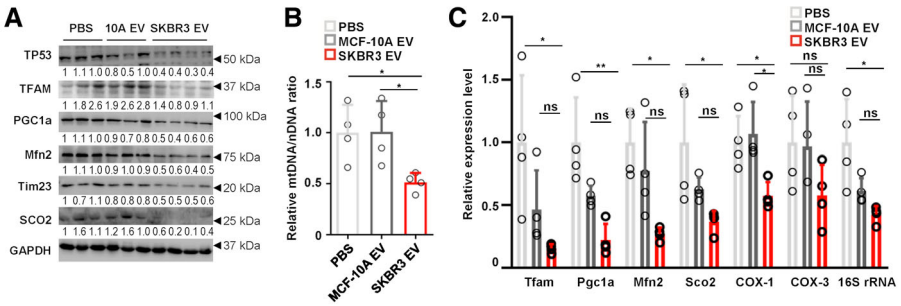

Figure 5. EVs from SKBR3 BC cells suppress the p53 pathway in skeletal muscle.

A GA was collected from female NSG mice that had received indicated EVs or PBS for 5 weeks. Western blot analysis showing protein levels of p53 and genes related to mitochondrial homeostasis and function.

B Relative mtDNA/nDNA ratio in GA determined by PCR (one-way ANOVA, $n = 4$ mice per group).

C RT–qPCR showing indicated mRNAs in GA of indicated groups of mice. Data were normalized to *Ppib* and compared to control group receiving PBS (one-way ANOVA, $n = 4$ mice per group).

Data information: In bar graphs, values are shown as mean ± SD. The boxes in the box-and-whiskers plots show the median (center line) and the quartile range (25–75%), and the whiskers extend from the quartile to the minimum and maximum values. *$P < 0.05$, **$P < 0.01$, ns: not significant. Western blot signals are quantified and normalized to Gapdh.

mammary fat pads as shown in Fig 4A–G. The TP53-expressing AAV8 or control AAV8-expressing GFP were injected into the GA of both sides twice during the entire experiments, first immediately following cancer cell injection, and then 1 month later. At 6 weeks after cancer cell implantation, tumor-bearing mice that had received TP53-expressing AAV8 showed higher levels of p53 and its target genes in the GA (Fig 6A and B), along with partially restored levels of mtDNA and mitochondrial content (Fig 6C and D), reduced ROS levels (Fig 6E), as well as improved running capacity (Fig 6F). Tumor growth, body weight, and the weight of skeletal muscle were not significantly altered by AAV-delivered TP53 (Fig 6G–I).

Discussion

Due to its complex pathology and clinical presentation, cachexia is believed to be underdiagnosed in all cancers, especially BC, which occurs more often in overweight and obese women. While ≥ 5% body weight loss is reported in ~31% of BC patients, based on any of the frequently practiced definitions (Fox *et al*, 2009; Argiles *et al*, 2014), only ~24% of BC patients do not suffer from cachexia. Thus, while cachexia incidence is higher in pancreatic and gastric cancer (Fox *et al*, 2009), due to the high BC incidence, the absolute number of cachectic BC patients is substantially higher, making it a profound public health problem. Clinical trials targeting pro-cachectic inflammatory cytokines have shown little benefit in cancer patients (Fearon *et al*, 2012, 2013; Reid *et al*, 2012; Naito, 2019), suggesting that a one-size-fits-all mechanism is unlikely for cancer-associated cachexia. Instead, various molecular events may mediate the complex clinical manifestations of cachexia, including weight loss, muscle wasting, anorexia, fatigue, etc., and these may vary according to tumor type, site, and mass (Fearon *et al*, 2012). Low muscle mass and poor muscle quality are reported in one-third of non-metastatic, newly diagnosed BC patients at diagnosis before chemotherapy or radiation (Caan *et al*, 2018), suggesting mechanisms related to cancer itself and independent of therapy. The extent of the association of low muscle mass with poor survival is similar in stages II and III BC (Caan *et al*, 2018), which argues against muscle loss simply being due to a more aggressive cancer; instead, it suggests that other tumor/host-intrinsic mechanisms, independent of tumor stage, contribute to muscle

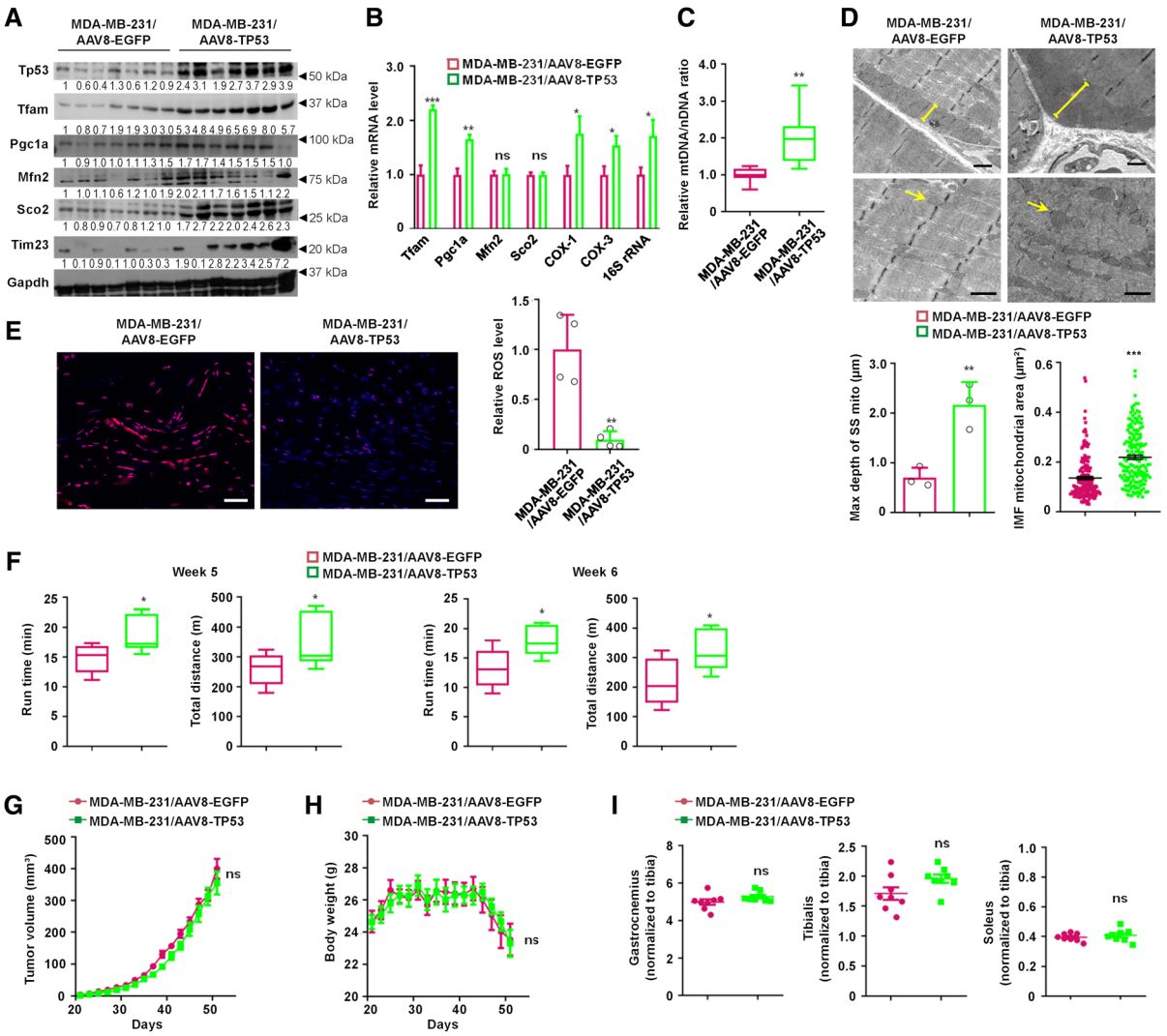

Figure 6. Exogenous TP53 expression in skeletal muscle rescues mitochondrial structure in tumor-bearing mice.

AAV8-TP53 virus or AAV8-eGFP control virus were injected into GA of both sides twice during the entire experiments, first immediately following implantation of MDA-MB-231 cells into the mammary fat pad, and then 1 month later. Muscles were collected at 6 weeks after tumor implantation.

A Western blot showing indicated protein levels in the GA.

B RT–qPCR showing relative levels of indicated genes in the GA (two-tailed Student's *t*-test, $n = 7$ mice per group).

C Relative mtDNA/nDNA ratio in GA determined by PCR (two-tailed Student's *t*-test, $n = 8$ mice per group).

D Representative TEM images showing SS and IMF mitochondria and their quantification in GA (two-tailed Student's *t*-test, $n = 3$ mice per group for the left subpanel and $n = 166$ or 181 mitochondria analyzed per group for the right subpanel). Scale bar: 1 μm. Yellow bars: depths of SS mitochondrial areas; arrows: IMF mitochondrial area.

E ROS levels in GA from indicated groups of mice. Quantified DHE signals were normalized to DAPI signals on the same section and used in analysis (two-tailed Student's *t*-test, $n = 4$ mice per group). Scale bar: 50 μm.

F Total running time and distance measured at weeks 5 and 6 in a run-to-exhaustion treadmill test (two-tailed Student's *t*-test, $n = 7$ for the AAV8-TP53 group and $n = 8$ for the AAV8-eGFP group).

G Tumor volume followed in all mice (two-tailed Student's *t*-test, $n = 8$ mice per group).

H Body weight followed in all mice (two-tailed Student's *t*-test, $n = 8$ mice per group).

I Weight of indicated skeletal muscle normalized to tibia length (two-tailed Student's *t*-test, $n = 8$ mice per group).

Data information: In all bar and line graphs, values are shown as mean ± SD. The boxes in the box-and-whiskers plots show the median (center line) and the quartile range (25–75%), and the whiskers extend from the quartile to the minimum and maximum values. $*P < 0.05$, $**P < 0.01$, $***P < 0.001$, ns: not significant. Western blot signals are quantified and normalized to Gapdh.

dysregulation. Our study here identifies a mechanism through miR-122 loaded in BC cell-derived EVs by targeting p53 pathway in the skeletal muscle, which leads to mitochondrial dysfunction and may contribute to muscle weakness in some cancer patients.

miR-122 has been reported to be transcriptionally suppressed by TGF-β/Smad signaling and, in turn, target TGF-β receptor-II, contributing to the regulation of TGF-β pathway in skeletal muscle fibrosis and myogenesis (Sun *et al*, 2018; Ding *et al*, 2020). However, since in

our mouse GA GSEA analysis, the TGF-β signaling pathway did not reach statistical significance ($P > 0.05$; Dataset EV1), we did not focus on the TGF-β pathway in EV-treated skeletal muscle. miRNAs are known to simultaneously regulate multiple target genes in a cellular context-dependent manner. Here, we focus on the p53 pathway because of the widely demonstrated relevance of p53 to mitochondrial dysregulation, which is observed in our study, and because of the potential significance of establishing a cancer-associated p53-supressing mechanism in p53-proficient non-cancer cells. Other miR-122-dependent and -independent mechanisms are expected to contribute to cancer-associated dysregulation of skeletal muscle. For example, we have previously reported that miR-122 targets glycolysis (Fong *et al*, 2015; Cao *et al*, 2022), which may directly or indirectly regulate energy homeostasis in skeletal muscle. In another recent study, we report that miR-122 targets O-GlcNAc transferase (OGT) to decrease O-GlcNAcylation and increase the protein abundance of ryanodine receptor 1 (Yan *et al*, 2022). This results in elevated cytosolic Ca^{2+} and calpain protease activation, promoting proteolysis and loss of muscle mass (Yan *et al*, 2022). The OGT-dependent mechanism, together with the herein reported p53-dependent mitochondrial dysregulation, represent two miR-122-mediated pathways in cancer-associated impairment of skeletal muscle homeostasis and function. Although restoration of p53 level did not seem to affect skeletal muscle mass, which could be more dependent on miR-122-induced proteolysis, these two pathways could have a synergistic effect by targeting two highly coordinated events in muscle function, namely Ca^{2+} flux and ATP generation. Meanwhile, therapeutic inhibition of miR-122 could be a promising strategy to rescue skeletal muscle function in some cases of cancer, which warrants further studies.

The tumor suppressor p53 has been extensively studied in the context of cancer as the "guardian of the genome" and the most frequently altered gene in human cancer (Levine & Oren, 2009). In addition to its well-known role as a transcription factor orchestrating gene expression in cell cycle arrest, senescence, and apoptosis in response to genotoxic stress, p53 also influences various metabolic pathways in response to metabolic stress and is profoundly implicated in metabolic diseases (Kruse & Gu, 2009; Berkers *et al*, 2013). In addition to its role in regulating mitochondrial homeostasis and function, which we investigated in this study, p53 has also been shown to modulate autophagy in a dual fashion. While nuclear p53 transactivates pro-apoptotic and pro-autophagic genes, cytoplasmic p53 can repress autophagy through an AMPK-dependent pathway (Tasdemir *et al*, 2008; White, 2016). Inhibition of p53 induces reticulophagy (autophagy of the ER) followed by mitophagy (autophagy of mitochondria) (Tasdemir *et al*, 2008). These potential downstream events of p53 signaling could also contribute to impaired skeletal muscle homeostasis, especially under stressed conditions, such as exercise and aging (Hood *et al*, 2019), for which further investigations are required. In our study, restoration of p53 expression in GA was able to reverse breast tumor's effects on muscle mitochondrial content and mouse running capacity but was not sufficient to affect skeletal muscle weight (Fig 6). This suggests that p53-independent pathways are required to drive skeletal muscle loss observed in cancer patients, whereas suppression of p53 may still play a contributing role.

Dysregulated cellular energetics in cancer cells is a cancer hallmark, and mitochondrial dysfunction is implicated in multiple aspects during cancer progression. Cancer cells harbor a variety of mechanisms leading to mitochondrial dysfunction, including alterations in mtDNA through point mutations and copy number changes, deregulated mitochondrial biogenesis and turnover as well as fission and fusion dynamics, and impaired mitochondrial respiratory chain due to defective mitochondrial enzymes (Wallace, 2005; Vyas *et al*, 2016). In addition to bioenergetics, mitochondrial dysfunction in cancer cells also impacts the regulation of oxidative stress, redox homeostasis, and cell death, which contribute to cancer invasiveness and resistance to therapies (Vyas *et al*, 2016). The pro-cancerous effect of *TP53* inactivation in cancer cells is known to be mediated by both transcription-dependent and -independent mechanisms, including loss of the pro-apoptotic function of cytoplasmic p53 that interacts with the Bcl-2 family to induce mitochondrial outer membrane permeabilization (Vaseva & Moll, 2009). As one of the most frequently mutated genes in human cancers, inactivation of *TP53* and its downstream signaling in cancer cells are unlikely to be mediated by miR-122, which is restricted at a low intracellular level in BC cells despite its high secretion into the EVs (Fong *et al*, 2015). Therefore, the mechanism identified herein would be relevant to non-cancer cells carrying wild-type *TP53* and an intact p53 signaling pathway and meanwhile susceptible to cancer cell-derived miR-122. Given the regulated but broad distribution of cancer-derived EVs (Becker *et al*, 2016), other organs in addition to skeletal muscle, such as brain and lungs, may undergo similar cancer-directed dysregulation of p53 signaling and mitochondrial function, which warrants further investigations.

Materials and Methods

Reagents and Tools table

Reagent/Resource	Reference or source	Identifier or catalog number	
Experimental models			
NSG (*M. musculus*)	Jackson Lab	NOD.Cg-Prkdcscid Il2rgtm1Wjl/SzJ	
BALB/c (*M. musculus*)	Jackson Lab	BALB/cJ	
Recombinant DNA			
pCEP4-p53	Addgene	Cat # 42512	
Antibodies			
Anti-Tp53	Novus Biologicals	NB200-103	1:1,000

Reagents and Tools table (continued)

Reagent/Resource	Reference or source	Identifier or catalog number	
Anti-Pgc1a	Proteintech	20658-1-AP	1:1,000
Anti-Tfam	Santa Cruz Biotechnology	sc-166965	1:500
Anti-Sco2	Proteintech	21223-1-AP	1:500
Anti-Tim23	BD Biosciences	611222	1:1,000
Anti-Mfn2	Cell Signaling Technology	9482S	1:1,000
Anti-Gapdh	Cell Signaling Technology	2118S	1:1,000
Anti-Alix	Cell Signaling Technology	92880S	1:1,000
Anti-TSG101	Invitrogen	PA5-31260	1:1,000
Anti-GM130	Cell Signaling Technology	12480S	1:1,000
Anti-CD9	Cell Signaling Technology	13403S	1:1,000
Myogenin rabbit pAb	Abclonal	Cat # A17427	1:100
Anti-human CD63 antibody	Novus Biologicals	Cat # NB100-77913	1:50
Alexa Fluor 594-conjugated goat anti-rabbit IgG	Invitrogen	Cat # A-11012	At 2 μg/ml final concentration
HyperFluor 488-conjugated goat anti-mouse IgG	APExBIO	Cat # K1204	1:500
Oligonucleotides and sequence-based reagents			
PCR primers		Sequence	
Mouse Tfam (Forward)	This study	CTGATGGGTATGGAGAAGGAGG	
Mouse Tfam (Reverse)	This study	CCAACTTCAGCCATCTGCTCTTC	
Mouse Mfn2 (Forward)	This study	TGACCTGAATTGTGACAAGCTG	
Mouse Mfn2 (Reverse)	This study	AGACTGACTGCCGTATCTGGT	
Mouse Ppargc1a/Pgc1α (Forward)	This study	AGACAAATGTGCTTCGAAAAAGAA	
Mouse Ppargc1a/Pgc1α (Reverse)	This study	GAAGAGATAAAGTTGTTGGTTTGGC	
Mouse Sco2 (Forward)	This study	AGCTCTCTCAGTTCAAACCCC	
Mouse Sco2 (Reverse)	This study	GCAGTCTAGTTCTTAGCCCAGG	
Mouse COX-1 (Forward)	This study	TGC TTA CAC CAC ATG AAA CA	
Mouse COX-1 (Reverse)	This study	TTTTTTTTTTTTTTTTTTTTTTTTTTTATTTT	
Mouse COX-3 (Forward)	This study	GAA GCC GCA GCA TGA TAC TG	
Mouse COX-3 (Reverse)	This study	TTTTTTTTTTTTTTTTTTTTTTTTTAAGATC	
Mouse 16S rRNA (Forward)	This study	CCGCAAGGGAAAGATGAAAGAC	
Mouse 16S rRNA (Reverse)	This study	TCGTTTGGTTTCGGGGTTTC	
Mouse Cyclophilin B/Ppib (Forward)	This study	GGAGATGGCACAGGAGGAA	
Mouse Cyclophilin B/Ppib (Reverse)	This study	GCCCGTAGTGCTTCAGCTT	
Mouse Nd1 (Forward)	This study	GTTGGTCCATACGGCATTTT	
Mouse Nd1 (Reverse)	This study	TGGCTGTGGTATTGGTAGCG	
Mouse Ppia (Forward)	This study	GCATACAGGTCCTGGCATCTTGTCC	
Mouse Ppia (Reverse)	This study	ATGGTGATCTTCTTGCTGGTCTTGC	
Chemicals, enzymes and other reagents			
Dulbecco's Modified Eagle's medium (DMEM)	Gibco	Cat # 11965092	
Fetal bovine serum (FBS)	Millipore-Sigma	Cat # F2442	
Horse serum	Gibco	Cat # 26050088	
X-tremeGENE™ HP DNA Transfection Reagent	Roche	Cat # XTGHP-RO	
Lipofectamine™ RNAiMAX Transfection Reagent	Thermo Fisher Scientific	Cat # 13778150	
MirVana® miR-122-5p mimic	Thermo Fisher Scientific	Cat # 4464066	
MirVana® negative control	Thermo Fisher Scientific	Cat # 4464061	
Ambion® Anti-miR™ miRNA inhibitors	Thermo Fisher Scientific	Cat # AM17000	

Reagents and Tools table (continued)

Reagent/Resource	Reference or source	Identifier or catalog number
Ambion® Anti-miR™ negative control	Thermo Fisher Scientific	Cat # AM17010
Attractene Transfection Reagent	Qiagen	Cat # 301005
Dual-Glo Luciferase Assay System	Promega	Cat # E2920
RIPA Lysis and Extraction Buffer	Thermo Scientific	Cat # 89901
cOmplete™ Protease Inhibitor Cocktail	Roche	Cat # 04693124001
Halt™ Phosphatase Inhibitor Single-Use Cocktail	Thermo Scientific	Cat # 78428
Pierce™ BCA Protein Assay Kit	Thermo Scientific	Cat # 23225
PVDF membrane	Bio-Rad	Cat # 1620177
Pierce™ ECL Western Blotting Substrate	Thermo Scientific	Cat # 32106
SuperSignal™ ELISA Pico Chemiluminescent Substrate	Thermo Scientific	Cat # 37069
Luminescent ATP Detection Assay Kit	Abcam	Cat # ab113849
DCFDA Cellular ROS Detection Assay Kit	Abcam	Cat # ab113851
Tissue-Tek® O.C.T. Compound	Sakura Finetek	Cat # 4583
DAPI	Sigma-Aldrich	Cat # D9564-10MG
Dihydroethidium (DHE) Sigma-Aldrich, Catalog # D7008-10MG	Sigma-Aldrich	Cat # D7008-10MG
Software		
ImageJ	https://github.com/imagej/ImageJ	
Image Pro Premier 9.3 software	https://my.mediacy.com/	
GSEA 3.0	https://www.gsea-msigdb.org/gsea/index.jsp	

Methods and Protocols

Cells and constructs

MDA-MB-231 and SKBR3 human BC cells, MCF-10A non-cancerous human mammary epithelial cells, 4T1 mouse mammary tumor cells, and C2C12 mouse myoblasts were obtained from the American Type Culture Collection (Manassas, VA). MDA-MB-231, SKBR3, and C2C12 cells were cultured in Dulbecco's Modified Eagle's medium (DMEM; Gibco, Catalog # 11965092) supplemented with 10% fetal bovine serum (FBS; Millipore-Sigma, Catalog # F2442). 4T1 cells were cultured in RPMI-1640 medium supplemented with 10% FBS. C2C12 myogenic differentiation was induced in DMEM supplemented with 2% horse serum (Gibco, Catalog # 26050088) for 4–7 days before treatment. Transient transfections of C2C12 myoblasts were performed immediately after plating freshly trypsinized cells using X-tremeGENE™ HP DNA Transfection Reagent (Roche, Catalog # XTGHP-RO) for DNA and Lipofectamine™ RNAiMAX Transfection Reagent (Thermo Fisher Scientific, Catalog # 13778150) for RNA. Twenty-four hours later, cells were switched to differentiation media. MCF-10A engineered to stably overexpress miR-122 (MCF-10A/miR-122) or the empty pBABE vector (MCF-10A/vec) was constructed previously (Fong *et al*, 2015) and cultured as described (Debnath *et al*, 2002). MDA-MB-231 and 4T1 cells with stable knockdown of *RAB27A* (MDA-MB-231/Rab27a KD and 4T1/Rab27a KD) or with CRISPR/Cas9-mediated knockout of miR-122 (MDA-MB-231/miR-122 KO and 4T1/miR-122 KO) were constructed previously as described (Shen *et al*, 2019; Yan *et al*, 2022). Four PCR primers (1. CCTCGAGGTCGACGGTATCGATAAGC; 2. TGGACTTCAGGTGGCTG CTATGAGCCCTGCTCC; 3. GGAGCAGGGCTCATAGCAGCCACCT GAAGTCCA; and 4. CGGATCCGGCCTTGCCGTTCCCTGGTTA) and pCEP4-p53 (Addgene #42512) (Anastasiou *et al*, 2011) were used to construct pCEP4-p53 (miR-122-site-mutant) plasmid carrying human TP53 cDNA with a silent mutation to destroy the miR-122-binding site without affecting the amino acid coding. Primers 1 and 2, as well as primers 3 and 4, were first used in the first round of PCR; the PCR products were mixed to be used as a template for the second round of PCR using primers 1 and 4. To construct psiCHECK2 reporter plasmids, a fragment containing miR-122 binding site was cloned from pCEP4-p53 (wild-type) or pCEP4-p53 (miR-122-site-mutant) plasmid by PCR using primers CCTCGAGGAAGAAACCACTGGATGGAGAA and ATTTGCGGCCGCGCTTCTGACGCACACCTATT. To construct TP53-expressing AAV, the eGFP regions in pscAAV-CMV-eGFP plasmid (Gray & Zolotukhin, 2011) was replaced with the TP53 cDNA region PCR amplified from plasmid pCEP4-p53 (miR-122-site-mutant) using primers AATACCGGTTGGAGGAGCCGCAGTCAGATCCTAG and TAATGTACATCAGTCTGAGTCAGGCCCTTCTGTC. The resulting construct pscAAV-CMV-TP53 was confirmed by sequencing. MirVana® miR-122-5p mimic and negative control (Catalog #4464066 and 4464061) as well as Ambion® Anti-miR™ miRNA inhibitors of miR-122-5p, miR-151-3p, miR-652-3p, miR-325-3p, and a negative control (Catalog # AM17000 and AM17010) were purchased from Thermo Fisher Scientific.

AAV production

Adeno-associated virus were produced by the Vector Development Core Laboratory at UC San Diego using pscAAV-CMV-eGFP and pscAAV-CMV-TP53 plasmids. The titer was determined by PCR. AAV serotype 8 was used to achieve robust transgene expression in

skeletal muscle. For mouse GA muscle injection, 5×10^{11} genome copy of AAV resuspended in 50 μl PBS was used.

EV purification and characterization

Extracellular vesicles were purified from conditioned medium (CM) as previously described (Zhou *et al*, 2014; Fong *et al*, 2015; Yan *et al*, 2018). Briefly, CM was collected from cultured cells grown in medium-containing vesicle-depleted serum for 48 h, and pre-cleared by centrifugation at 500 *g* for 15 min, and then at 10,000 *g* for 20 min. EVs were pelleted by ultracentrifugation at 110,000 *g* for 70 min, and washed in PBS using the same ultracentrifugation conditions. When indicated, CFSE (5-(and 6)-Carboxyfluorescein diacetate succinimidyl ester of CFDA SE; BioLegend, San Diego, CA) was added into the PBS at 5 μM and incubated for 1 h at 37°C before the washing step, followed by an extra round of washing in PBS to remove the excess dye. The EV pellet was suspended in PBS and subjected to various experiments. Nanoparticle tracking analysis (NTA) was performed using a NanoSight NS300 (Malvern Panalytical; Westborough, MA). EV treatment with proteinase K (10 μg/ml) followed by RNase If (40 U) in the presence or absence of 1% Triton X-100 to determine the topology of EV RNA was performed as described (Shurtleff *et al*, 2017). For cell treatment, 2 μg of EVs (equivalent to those derived from ~5×10^6 producer cells) based on protein measurement using BCA protein assay kit (Thermo Fisher Scientific) were added to 2×10^5 recipient cells grown in 2 ml medium in a 6-well plate. When needed, EV treatment was done in a 96-well plate with proportionally reduced amounts of EVs and cell numbers.

Luciferase reporter assay

For luciferase reporter assay, 500 ng of psiCHECKs reporter plasmid DNA and 20 nM of miR-122-5p mimic or control (Thermo Fisher Scientific, Catalog #4464066 and 4464061) were co-transfected into 1×10^5 C2C12 myotubes grown in a 24-well plate using Attractene Transfection Reagent (Qiagen, Catalog # 301005) following manufacturer's procedures. *Firefly* and *Renilla* luciferase activities were determined 48 h post-transfection using the Dual-Glo Luciferase Assay System (Promega, Catalog # E2920).

RNA extraction and quantitative PCR with reverse transcription

These procedures were carried out as reported in Fong *et al* (2015), Yan *et al* (2018) and Zhou *et al* (2014). Sequences of the primers were obtained from PrimerBank and listed in Reagent Table. For mRNA detection, reverse transcription (RT) was performed using random primers and *Ppib* mRNA was used as an internal reference in PCR to calculate the relative level of each mRNA. For miRNA detection, TaqMan® miRNA assays were used, with gene-specific RT primers, TaqMan probes, and PCR primers. U6 was used as an internal reference for intracellular miRNA levels. As a spike-in reference for EV miRNA levels, 10 fmol of synthetic ath-miR159a was added during RNA extraction and measured for data normalization.

Western blot analysis

Cells were lysed in RIPA Lysis and Extraction Buffer (Thermo Scientific, Catalog # 89901) supplemented with cOmplete™ Protease Inhibitor Cocktail (Roche, Catalog # 04693124001) and Halt™ Phosphatase Inhibitor Single-Use Cocktail (Thermo Scientific, Catalog # 78428). Muscle tissues were homogenized in protease and phosphatase inhibitor-supplemented RIPA buffer using a Precellys 24 tissue homogenizer (Bertin Technologies). Protein concentrations in cell and tissue lysates were measured using the Pierce™ BCA Protein Assay Kit (Thermo Scientific, Catalog # 23225). An equal amount of protein extracts (~30 μg) were subjected to electrophoresis on a 10 or 12% SDS-polyacrylamide gel and then transferred onto a PVDF membrane (Bio-Rad, Catalog # 1620177). Protein detection was performed using antibodies described in Reagent Table. Horseradish peroxidase-conjugated secondary antibodies were used for all Western blots. Signals were detected using Pierce™ ECL Western Blotting Substrate (Thermo Scientific, Catalog # 32106) or SuperSignal™ ELISA Pico Chemiluminescent Substrate (Thermo Scientific, Catalog # 37069).

Measurements of mtDNA/nDNA ratio, intracellular ATP, and ROS levels

Relative mtDNA/nDNA ratio in GA was determined by PCR using primers of *Nd1* for mitochondrial DNA (mtDNA), and *Ppia* for nuclear DNA (nDNA). Intracellular ATP levels were measured using the Luminescent ATP Detection Assay Kit (Abcam, Cambridge, United Kingdom; Catalog # ab113849) following manufacturer's protocol. C2C12 myotubes grown and treated in a 96-well plate were lysed in 50 μl detergent and incubated with 50 μl substrate solution. Determined ATP levels were normalized to cell numbers. Cellular ROS levels were measured using the DCFDA Cellular ROS Detection Assay Kit (Abcam; Catalog # ab113851) following manufacturer's protocol. To detect ROS *in situ* in muscle sections, freshly dissected muscle tissues were embedded in Tissue-Tek® O.C.T. Compound (Sakura Finetek, Catalog # 4583), frozen, and sectioned into 5-μm-thick tissue sections. After staining with PBS containing 300 nM DAPI (Sigma-Aldrich, Catalog # D9564-10MG) in dark for 3 min and washing in PBS for three times, tissue sections were stained with PBS containing 10 μM dihydroethidium (DHE; Sigma-Aldrich, Catalog # D7008-10MG) in dark for 1 h and washed with PBS three times. Fluorescent microscope images were obtained for quantification of fluorescence intensity using ImageJ (National Institutes of Health).

Immunofluorescence

O.C.T. sections were fixed with 4% paraformaldehyde in PBS, blocked, and permeabilized with PBS containing 10% goat serum and 0.05% saponin, prior to incubation with Myogenin rabbit pAb diluted at 1:100 (ABclonal; Catalog # A17427) together with mouse anti-human CD63 antibody diluted at 1:50 (MEM-259; Novus Biologicals, Catalog # NB100-77913). Primary antibodies were then visualized with Alexa Fluor 594-conjugated goat anti-rabbit IgG at 2 μg/ml final concentration (Invitrogen, Catalog # A-11012) and HyperFluor 488-conjugated goat anti-mouse IgG diluted at 1:500 (APExBIO, Catalog # K1204). Nuclei were stained with 300 nM DAPI in PBS. Images were obtained using a ZEISS LSM 880 confocal microscope system (Carl Zeiss, Oberkochen, Germany) and processed using Image Pro Premier 9.3 software (Media Cybernetics, Rockville, MD).

EM of skeletal muscle

Gastrocnemius was dissected and fixed with 2% paraformaldehyde and 2.5% glutaraldehyde in 0.15 M sodium cacodylate buffer (SC buffer; pH 7.4). Samples were then treated with 1% osmium in 0.15 M SC buffer for 1–2 h on ice and washed in 0.15 M SC buffer. Then, samples were incubated in 2% of uranyl acetate for 1–2 h at

4°C, and sequentially dehydrated in ETOH of 50, 70, 90, and 100% and lastly in acetone. After that, samples were incubated in 50:50 ETOH:Durcupan for > 1 h at room temperature, and then in 100% Durcupan overnight. Tissues were embedded in Durcupan in a 60°C oven for 36–48 h. Ultrathin sections (60 nm) were cut using a Leica microtome with diamond knife and followed by post-staining with both uranyl acetate and lead. Images were captured on a JEOL 1400 plus TEM at 80 kV with Gatan 4k × 4k camera.

Animals

All animal experiments were approved by the Institutional Animal Care and Use Committee at the University of California, San Diego. This study is compliant with all relevant ethical regulations regarding animal research. Female NOD/SCID/IL2Rγ-null (NSG) mice (for EV injection and MDA-MB-231 tumor models) and BALB/c mice (for 4T1 tumor model) of ~8-week-old were used at a facility that maintains a 12:12 h light/dark cycle with Zeitgeber time (ZT) 12 = lights off. EVs were injected into the tail vein semiweekly for 5 weeks (~10 μg EVs per injection per mouse). In our previous study, a similar dose of i.v. injected BC-derived EVs results in higher serum levels of BC-secreted miRNA that are comparable to mice carrying mammary tumors that naturally secrete the miRNA (Fong *et al*, 2015). Following the last EV treatment, bioenergetics was analyzed by using the comprehensive laboratory animal monitoring system (CLAMS; Columbus Instruments). Oxygen consumption (VO2) and carbon dioxide production (VCO2) were measured, and the respiratory exchange ratio is calculated as VCO2/VO2. Ambient temperature for all experiments was 22–24°C. MDA-MB-231 and 4T1 tumors were established by injecting 2×10^5 wild-type (control) cells, Rab27a KD cells, or miR-122 KO cells mixed with Matrigel (BD Biosciences; San Jose, CA) into the No. 4 mammary fat pad. For p53 restoration in skeletal muscle, 5×10^{11} genomic copy of AAV8-CMV-TP53 virus or control AAV8-CMV-eGFP virus were injected into GA of both sides immediately following implantation of MDA-MB-231 cells into the mammary fat pad. One month later, viruses were injected again. For high-intensity treadmill running test, mice were acclimated to the treadmill 4–5 days prior to the exercise test session. The test was conducted on an open-field six-lane treadmill (Eco 3/6; Columbus Instruments) set at a 10% incline. Following a 5-min 10 m/min acclimation period, the speed was increased by 2 m/min every 2 min to a maximal pace of 30 m/min until exhaustion (DeBalsi *et al*, 2014). Mice ran to exhaustion, defined as 10 consecutive seconds on the shock grid.

RNA-seq and GSEA

RNA sequencing and data analysis were carried out by Novogene (Sacramento, CA). RNA libraries were prepared for sequencing using standard Illumina protocols. mRNA was purified from total RNA using poly-T oligo-attached magnetic beads, and was fragmented randomly by addition of fragmentation buffer. Downstream analysis was performed using a combination of programs including STAR, HTseq, Cufflink, and Novogene's wrapped scripts. Alignments were parsed using Tophat program and differential expressions were determined through DESeq2/edgeR. Reference genome and gene model annotation files were downloaded from genome website browser (NCBI/UCSC/Ensembl) directly. Indexes of the reference genome was built using STAR and paired-end clean reads were aligned to the reference genome using STAR (v2.5). STAR used the method of maximal mappable prefix (MMP) which can generate a precise mapping result for junction reads. HTSeq v0.6.1 was used to count the read numbers mapped of each gene. And then FPKM (fragments per kilobase million) of each gene was calculated based on the length of the gene and reads count mapped to this gene. For GSEA, FPKM were uploaded to GSEA 3.0 and enrichment of gene sets was interrogated with 1,000 random permutations to obtain the normalized enrichment score (NES), *P*-value, and *q*-value.

Statistics and reproducibility

Quantitative data are presented as mean ± standard deviation (SD). Two-tailed Student's *t*-tests were used for comparison of means of data between two groups. For multiple independent groups, one-way ANOVA with *post hoc* Tukey tests were used. Values of $P < 0.05$ were considered significant. Sample size was generally chosen based on preliminary data, indicating the variance within each group and the differences between groups. All samples that have received the proper procedures with confidence were included for the analyses. Animals were randomized before treatments. Randomization was performed by assigning random numbers from random number tables to the treatment conditions. Western blots were repeated independently for at least two times with similar results, and representative images are shown.

Data availability

The datasets produced in this study are available in the following databases: RNA-Seq data: Gene Expression Omnibus GSE156909 (https://www.ncbi.nlm.nih.gov/geo/query/acc.cgi?acc=GSE156909); RNA-Seq data: Gene Expression Omnibus GSE164303 (https://www.ncbi.nlm.nih.gov/geo/query/acc.cgi?acc=GSE164303); Source data for the study have been uploaded to BioStudies with the accession code S-BSST1090 (https://www.ebi.ac.uk/biostudies/studies/S-BSST1090).

Expanded View for this article is available online.

Acknowledgements

This work was supported by the National Institutes of Health (NIH) grants R56AR080153 (SEW & SS), R01CA218140 (SEW), R01CA206911 (SEW), R01CA266486 (SEW), R21AR072882 (SS), R21AR069775 (SS), R01HL091071 (HHP), R01HL138560 (ÅBG), R01HL132300 (ÅBG), TRDRP 27IR-0013 (ÅBG), and the Veterans Administration BX001963 (HHP) and BX005229 (HHP). Research reported in this publication included work performed in the core facilities supported by the NIH under grant number P30CA23100 (UC San Diego Moores Cancer Center).

Author contributions

Xianhui Ruan: Data curation; formal analysis; validation; methodology; writing – original draft; writing – review and editing. **Minghui Cao:** Formal analysis; methodology. **Wei Yan:** Formal analysis; methodology. **Ying Z Jones:** Formal analysis; methodology. **Åsa B Gustafsson:** Conceptualization; methodology; writing – original draft. **Hemal H Patel:** Conceptualization; methodology; writing – original draft. **Simon Schenk:** Conceptualization; supervision; funding acquisition; writing – original draft. **Shizhen Emily Wang:** Conceptualization; resources; software; formal analysis; supervision; funding acquisition; investigation; methodology; writing – original draft; project administration; writing – review and editing.

Disclosure and competing interests statement

The authors declare that they have no conflict of interest.

References

Anastasiou D, Poulogiannis G, Asara JM, Boxer MB, Jiang JK, Shen M, Bellinger G, Sasaki AT, Locasale JW, Auld DS *et al* (2011) Inhibition of pyruvate kinase M2 by reactive oxygen species contributes to cellular antioxidant responses. *Science* 334: 1278 – 1283

Aquilano K, Baldelli S, Pagliei B, Cannata SM, Rotilio G, Ciriolo MR (2013) p53 orchestrates the PGC-1alpha-mediated antioxidant response upon mild redox and metabolic imbalance. *Antioxid Redox Signal* 18: 386 – 399

Argiles JM, Busquets S, Stemmler B, Lopez-Soriano FJ (2014) Cancer cachexia: understanding the molecular basis. *Nat Rev Cancer* 14: 754 – 762

Becker A, Thakur BK, Weiss JM, Kim HS, Peinado H, Lyden D (2016) Extracellular vesicles in cancer: cell-to-cell mediators of metastasis. *Cancer Cell* 30: 836 – 848

Benediktsson AM, Schachtele SJ, Green SH, Dailey ME (2005) Ballistic labeling and dynamic imaging of astrocytes in organotypic hippocampal slice cultures. *J Neurosci Methods* 141: 41 – 53

Berkers CR, Maddocks OD, Cheung EC, Mor I, Vousden KH (2013) Metabolic regulation by p53 family members. *Cell Metab* 18: 617 – 633

Caan BJ, Cespedes Feliciano EM, Prado CM, Alexeeff S, Kroenke CH, Bradshaw P, Quesenberry CP, Weltzien EK, Castillo AL, Olobatuyi TA *et al* (2018) Association of muscle and adiposity measured by computed tomography with survival in patients with nonmetastatic breast cancer. *JAMA Oncol* 4: 798 – 804

Cao M, Isaac R, Yan W, Ruan X, Jiang L, Wan Y, Wang J, Wang E, Caron C, Neben S *et al* (2022) Cancer-cell-secreted extracellular vesicles suppress insulin secretion through miR-122 to impair systemic glucose homeostasis and contribute to tumour growth. *Nat Cell Biol* 24: 954 – 967

DeBalsi KL, Wong KE, Koves TR, Slentz DH, Seiler SE, Wittmann AH, Ilkayeva OR, Stevens RD, Perry CG, Lark DS *et al* (2014) Targeted metabolomics connects thioredoxin-interacting protein (TXNIP) to mitochondrial fuel selection and regulation of specific oxidoreductase enzymes in skeletal muscle. *J Biol Chem* 289: 8106 – 8120

Debnath J, Mills KR, Collins NL, Reginato MJ, Muthuswamy SK, Brugge JS (2002) The role of apoptosis in creating and maintaining luminal space within normal and oncogene-expressing mammary acini. *Cell* 111: 29 – 40

Ding Z, Lin J, Sun Y, Cong S, Liu S, Zhang Y, Chen Q, Chen J (2020) miR-122-5p negatively regulates the transforming growth factor-beta/Smad signaling pathway in skeletal muscle myogenesis. *Cell Biochem Funct* 38: 231 – 238

Donahue RJ, Razmara M, Hoek JB, Knudsen TB (2001) Direct influence of the p53 tumor suppressor on mitochondrial biogenesis and function. *FASEB J* 15: 635 – 644

Fearon KC, Glass DJ, Guttridge DC (2012) Cancer cachexia: mediators, signaling, and metabolic pathways. *Cell Metab* 16: 153 – 166

Fearon K, Arends J, Baracos V (2013) Understanding the mechanisms and treatment options in cancer cachexia. *Nat Rev Clin Oncol* 10: 90 – 99

Fong MY, Zhou W, Liu L, Alontaga AY, Chandra M, Ashby J, Chow A, O'Connor ST, Li S, Chin AR *et al* (2015) Breast-cancer-secreted miR-122 reprograms glucose metabolism in premetastatic niche to promote metastasis. *Nat Cell Biol* 17: 183 – 194

Fox KM, Brooks JM, Gandra SR, Markus R, Chiou CF (2009) Estimation of cachexia among cancer patients based on four definitions. *J Oncol* 2009: 693458

Gray JT, Zolotukhin S (2011) Design and construction of functional AAV vectors. *Methods Mol Biol* 807: 25 – 46

Griffiths EJ, Rutter GA (2009) Mitochondrial calcium as a key regulator of mitochondrial ATP production in mammalian cells. *Biochim Biophys Acta* 1787: 1324 – 1333

He WA, Calore F, Londhe P, Canella A, Guttridge DC, Croce CM (2014) Microvesicles containing miRNAs promote muscle cell death in cancer cachexia via TLR7. *Proc Natl Acad Sci USA* 111: 4525 – 4529

Hood DA, Memme JM, Oliveira AN, Triolo M (2019) Maintenance of skeletal muscle mitochondria in health, exercise, and aging. *Annu Rev Physiol* 81: 19 – 41

Kruse JP, Gu W (2009) Modes of p53 regulation. *Cell* 137: 609 – 622

Levine AJ, Oren M (2009) The first 30 years of p53: growing ever more complex. *Nat Rev Cancer* 9: 749 – 758

Lowell BB, Shulman GI (2005) Mitochondrial dysfunction and type 2 diabetes. *Science* 307: 384 – 387

Matoba S, Kang JG, Patino WD, Wragg A, Boehm M, Gavrilova O, Hurley PJ, Bunz F, Hwang PM (2006) p53 regulates mitochondrial respiration. *Science* 312: 1650 – 1653

Montgomery MK, Turner N (2015) Mitochondrial dysfunction and insulin resistance: an update. *Endocr Connect* 4: R1 – R15

Naito T (2019) Emerging treatment options for cancer-associated cachexia: a literature review. *Ther Clin Risk Manag* 15: 1253 – 1266

Noone AM, Howlader N, Krapcho M, Miller D, Brest A, Yu M, Ruhl J, Tatalovich Z, Mariotto A, Lewis DR *et al* (2018) SEER Cancer Statistics Review, 1975-2015, National Cancer Institute. Bethesda, MD, https://seer.cancer.gov/csr/1975_2015/, based on November 2017 SEER data submission, posted to the SEER web site, April 2018. National Cancer Institute

Ostrowski M, Carmo NB, Krumeich S, Fanget I, Raposo G, Savina A, Moita CF, Schauer K, Hume AN, Freitas RP *et al* (2010) Rab27a and Rab27b control different steps of the exosome secretion pathway. *Nat Cell Biol* 12: 19 – 30

Pamoukdjian F, Bouillet T, Levy V, Soussan M, Zelek L, Paillaud E (2018) Prevalence and predictive value of pre-therapeutic sarcopenia in cancer patients: a systematic review. *Clin Nutr* 37: 1101 – 1113

Park JY, Wang PY, Matsumoto T, Sung HJ, Ma W, Choi JW, Anderson SA, Leary SC, Balaban RS, Kang JG *et al* (2009) p53 improves aerobic exercise capacity and augments skeletal muscle mitochondrial DNA content. *Circ Res* 105: 705 – 712

Prado CM, Baracos VE, McCargar LJ, Reiman T, Mourtzakis M, Tonkin K, Mackey JR, Koski S, Pituskin E, Sawyer MB (2009) Sarcopenia as a determinant of chemotherapy toxicity and time to tumor progression in metastatic breast cancer patients receiving capecitabine treatment. *Clin Cancer Res* 15: 2920 – 2926

Reid J, Mills M, Cantwell M, Cardwell CR, Murray LJ, Donnelly M (2012) Thalidomide for managing cancer cachexia. *Cochrane Database Syst Rev* 2012: CD008664

Rier HN, Jager A, Sleijfer S, van Rosmalen J, Kock M, Levin MD (2017) Low muscle attenuation is a prognostic factor for survival in metastatic breast cancer patients treated with first line palliative chemotherapy. *Breast* 31: 9 – 15

Ruas JL, White JP, Rao RR, Kleiner S, Brannan KT, Harrison BC, Greene NP, Wu J, Estall JL, Irving BA *et al* (2012) A PGC-1alpha isoform induced by resistance training regulates skeletal muscle hypertrophy. *Cell* 151: 1319 – 1331

Saleem A, Adhihetty PJ, Hood DA (2009) Role of p53 in mitochondrial biogenesis and apoptosis in skeletal muscle. *Physiol Genomics* 37: 58 – 66

Saleem A, Iqbal S, Zhang Y, Hood DA (2015) Effect of p53 on mitochondrial morphology, import, and assembly in skeletal muscle. *Am J Physiol Cell Physiol* 308: C319 – C329

Shachar SS, Deal AM, Weinberg M, Nyrop KA, Williams GR, Nishijima TF, Benbow JM, Muss HB (2017) Skeletal muscle measures as predictors of toxicity, hospitalization, and survival in patients with metastatic breast cancer receiving taxane-based chemotherapy. *Clin Cancer Res* 23: 658 – 665

Shen M, Dong C, Ruan X, Yan W, Cao M, Pizzo D, Wu X, Yang L, Liu L, Ren X *et al* (2019) Chemotherapy-induced extracellular vesicle miRNAs promote breast cancer stemness by targeting ONECUT2. *Cancer Res* 79: 3608 – 3621

Shurtleff MJ, Yao J, Qin Y, Nottingham RM, Temoche-Diaz MM, Schekman R, Lambowitz AM (2017) Broad role for YBX1 in defining the small noncoding RNA composition of exosomes. *Proc Natl Acad Sci USA* 114: E8987 – E8995

Siegel RL, Miller KD, Jemal A (2018) Cancer statistics, 2018. *CA Cancer J Clin* 68: 7 – 30

Stocks B, Dent JR, Joanisse S, McCurdy CE, Philp A (2017) Skeletal muscle fibre-specific knockout of p53 does not reduce mitochondrial content or enzyme activity. *Front Physiol* 8: 941

Sun Y, Wang H, Li Y, Liu S, Chen J, Ying H (2018) miR-24 and miR-122 negatively regulate the transforming growth factor-beta/Smad signaling pathway in skeletal muscle fibrosis. *Mol Ther Nucleic Acids* 11: 528 – 537

Tasdemir E, Maiuri MC, Galluzzi L, Vitale I, Djavaheri-Mergny M, D'Amelio M, Criollo A, Morselli E, Zhu C, Harper F *et al* (2008) Regulation of autophagy by cytoplasmic p53. *Nat Cell Biol* 10: 676 – 687

Vaseva AV, Moll UM (2009) The mitochondrial p53 pathway. *Biochim Biophys Acta* 1787: 414 – 420

Villasenor A, Ballard-Barbash R, Baumgartner K, Baumgartner R, Bernstein L, McTiernan A, Neuhouser ML (2012) Prevalence and prognostic effect of sarcopenia in breast cancer survivors: the HEAL study. *J Cancer Surviv* 6: 398 – 406

Vyas S, Zaganjor E, Haigis MC (2016) Mitochondria and cancer. *Cell* 166: 555 – 566

Wallace DC (2005) A mitochondrial paradigm of metabolic and degenerative diseases, aging, and cancer: a dawn for evolutionary medicine. *Annu Rev Genet* 39: 359 – 407

Wang B, Wang H, Yang Z (2012) MiR-122 inhibits cell proliferation and tumorigenesis of breast cancer by targeting IGF1R. *PloS One* 7: e47053

Waning DL, Mohammad KS, Reiken S, Xie W, Andersson DC, John S, Chiechi A, Wright LE, Umanskaya A, Niewolna M *et al* (2015) Excess TGF-beta mediates muscle weakness associated with bone metastases in mice. *Nat Med* 21: 1262 – 1271

Wen S, Gao J, Zhang L, Zhou H, Fang D, Feng S (2016) p53 increase mitochondrial copy number via up-regulation of mitochondrial transcription factor A in colorectal cancer. *Oncotarget* 7: 75981 – 75995

White E (2016) Autophagy and p53. *Cold Spring Harb Perspect Med* 6: a026120

Wilson HE, Rhodes KK, Rodriguez D, Chahal I, Stanton DA, Bohlen J, Davis M, Infante AM, Hazard-Jenkins H, Klinke DJ *et al* (2019) Human breast cancer xenograft model implicates peroxisome proliferator-activated receptor signaling as driver of cancer-induced muscle fatigue. *Clin Cancer Res* 25: 2336 – 2347

Wilson HE, Stanton DA, Montgomery C, Infante AM, Taylor M, Hazard-Jenkins H, Pugacheva EN, Pistilli EE (2020) Skeletal muscle reprogramming by breast cancer regardless of treatment history or tumor molecular subtype. *NPJ Breast Cancer* 6: 18

Wu X, Somlo G, Yu Y, Palomares MR, Li AX, Zhou W, Chow A, Yen Y, Rossi JJ, Gao H *et al* (2012) *De novo* sequencing of circulating miRNAs identifies novel markers predicting clinical outcome of locally advanced breast cancer. *J Transl Med* 10: 42

Yan W, Wu X, Zhou W, Fong MY, Cao M, Liu J, Liu X, Chen CH, Fadare O, Pizzo DP *et al* (2018) Cancer-cell-secreted exosomal miR-105 promotes tumour growth through the MYC-dependent metabolic reprogramming of stromal cells. *Nat Cell Biol* 20: 597 – 609

Yan W, Cao M, Ruan X, Jiang L, Lee S, Lemanek A, Ghassemian M, Pizzo DP, Wan Y, Qiao Y *et al* (2022) Cancer-cell-secreted miR-122 suppresses O-GlcNAcylation to promote skeletal muscle proteolysis. *Nat Cell Biol* 24: 793 – 804

Zhang G, Liu Z, Ding H, Zhou Y, Doan HA, Sin KWT, Zhu ZJ, Flores R, Wen Y, Gong X *et al* (2017) Tumor induces muscle wasting in mice through releasing extracellular Hsp70 and Hsp90. *Nat Commun* 8: 589

Zhou W, Fong MY, Min Y, Somlo G, Liu L, Palomares MR, Yu Y, Chow A, O'Connor ST, Chin AR *et al* (2014) Cancer-secreted miR-105 destroys vascular endothelial barriers to promote metastasis. *Cancer Cell* 25: 501 – 515

